Growth Dynamics of Faceted Al13Fe4 intermetallic Revealed by High-speed Synchrotron X-ray Quantification

Song, Zihan; Magdysyuk, Oxana; Tang, Lei; Sparks, Tay; Cai, Biao

DOI:
10.1016/j.jallcom.2021.158604

Document Version
Peer reviewed version

Citation for published version (Harvard):
Song, Z, Magdysyuk, O, Tang, L, Sparks, T & Cai, B 2021, 'Growth Dynamics of Faceted Al13Fe4 intermetallic Revealed by High-speed Synchrotron X-ray Quantification', *Journal of Alloys and Compounds*, vol. 861, 158604. https://doi.org/10.1016/j.jallcom.2021.158604

Growth Dynamics of Faceted $Al_{13}Fe_4$ intermetallic Revealed by High-speed Synchrotron X-ray Quantification

Zihan Song [a], Oxana V. Magdysyuk [b], Lei Tang [a], Tay Sparks[a], Biao Cai [a, *]

a. School of Metallurgy and Materials, University of Birmingham, Birmingham, UK
b. Diamond Light Source Ltd, Harwell Science and Innovation Campus, Didcot, UK

Corresponding author: Biao Cai (b.cai@bham.ac.uk)

Abstract:

High-speed synchrotron tomography was used to investigate the nucleation and growth dynamics of $Al_{13}Fe_4$ intermetallic during solidification of an Al-5wt%Fe alloy, providing new insights into its formation process. The majority of $Al_{13}Fe_4$ intermetallics nucleated near the surface oxide of the specimen and a few nucleated at $Al_{13}Fe_4$ phase. $Al_{13}Fe_4$ crystals grew into a variety of shapes, including plate-like, hexagonal tabular, stair-like and V-shaped, which can be attributed to the crystal structure of this compound and its susceptibility to twinning. Hole-like defects filled with aluminium melt were observed within the intermetallics. Orented particle attachment mechanism was proposed to explain the formation of the $Al_{13}Fe_4$ intermetalic, which needs further experiments and simulation to confirm.

Key words: Synchrotron tomography; 4D imaging; Al alloy; Faceted crystal

1. Introduction

During solidification of metallic alloys, intermetallic compounds can form with complex crystal structures that commonly show anisotropic faceted morphologies, which significantly influence the mechanical and functional properties of the materials [1–3]. Therefore, faceted intermetallics have been extensively studied, and there is renewed interest in developing intermetallic materials for engineering applications [4–6]. Additionally, faceted crystals can form during a wide range of chemical and physical processes, ranging from electrochemical reactions [7], the freezing of water [8,9] to the crystallization of magmas [10]. Thus, new insights into faceted crystal growth could have significant impacts on a range of subjects encompassing materials science, chemistry and geology.

Aluminium (Al) alloys are used in many applications ranging from mobile phones to cars and aeroplanes. During solidification of Al alloys, many faceted intermetallics such as β-Al_5FeSi, $Al_{13}Fe_4$ (or named as Al_3Fe), Al_6Mn and Al_3Ni can form [11–15]. Due to the difficulty of removing Fe from Al alloys and the low solubility of Fe in Al, Fe-enriched intermetallics are common in many Al alloys, which are detrimental to the mechanical and corrosion resistance performance [16–18]. This has become a more serious issue in recycled Al alloys as Fe accumulates within the alloy during recycling. Continuous research efforts have been focused on understanding Fe-rich intermetallic

formation during Al alloy solidification, such as α and β phase in Al-Si or Al-Si-Cu based alloys [19,20] and $Al_{13}Fe_4$ in Al-Fe alloys [21–23].

Many previous studies used post-mortem characterization methods (such as electron and optical microscopies or X-ray tomography) to determine the faceted morphology of the intermetallic compounds (e.g. Al_8Mn_5 and $Al_{13}Fe_4$) in Al or Mg-Al alloys [24–26] which could not reveal the dynamic formation processes. *In situ* X-ray radiography was used to capture the formation and evolution of α-Al(FeMnCr)Si [27,28] and β-Al_5FeSi [29] intermetallic phases in iron-containing Al-Si/Al-Si-Cu alloys, which allows the growth dynamics to be determined, but provides limited information regarding on their 3D morphology. High-speed synchrotron tomographic imaging, which capture tomograms in seconds or sub-seconds [30], enables time-resolved characterization of Fe-enriched intermetallics in 3D (termed as 4D imaging [31–35]). Much research focused on the β-Al_5FeSi phase [19,33,36], as it plays an important role in the mechanical performance of Al-Si based Al alloys. However, the plate-shaped β intermetallics are very thin [37] and as a result of its 3D morphology has not been resolved clearly by high-speed synchrotron X-ray tomography which usually has relatively low spatial resolutions (a few μm [38,39]). $Al_{13}Fe_4$ intermetallic in Al-Fe alloys, on the other hand, could grow into large faceted morphology [40], potentially resolvable by high-speed synchrotron tomography. We are interested in $Al_{13}Fe_4$ phase as currently *in situ* observation of $Al_{13}Fe_4$ formation has not been reported and this phase is known to form various shapes during solidification [41] while the exact mechanisms for the shape variation have not been clearly understood, meaning *in situ* observation of $Al_{13}Fe_4$ formation is of significant interest.

In the present study, high-speed synchrotron tomography was performed to investigate the nucleation and growth dynamics of $Al_{13}Fe_4$ intermetallics during Al-5wt%Fe alloy solidification. Quantifications of the synchrotron tomography provide details of the formation process of the intermetallic and establish a link between the morphology and the crystal structure, yielding new insights into faceted crystal growth mechanisms.

2. Materials and Methods

Sample preparation

An Al-5wt% Fe alloy was prepared from Al-20wt% Fe master alloys and pure (higher than 99.9%) aluminium. The materials were melted in a graphite crucible using electrical resistance heating at around 750℃ and held for half an hour to ensure all materials were fully melted. The alloys were then cast into a preheated mild-steel mould. Finally, cylindrical specimens with 1.8 mm diameter and 100 mm length were machined from the as-cast alloy via wire electrical discharge machining.

The *in situ* solidification experiment was performed at I12 beamline at the Diamond Light Source, Oxford with 55 keV monochromatic X-ray beam [38]. Module 3 out of four optical modules coupled with a PCO.edge camera (PCO AG, Germany) was used, providing pixel sizes of 3.24 × 3.24 μm^2. Images are cropped to 1080×1394 pixels,

resulting in a frame rate of 200 frames per second. During solidification, high-speed tomographic scans were captured as the sample was continuously rotated. Each tomogram required a collection time of 5 seconds and was composed of 1000 projections (radiograph), collected over a range of 180°. Another 5 seconds waiting time was required for downloading the tomogram between two consecutive scans.

A bespoke temperature gradient furnace [30,31] was used to perform the solidification experiment, as shown in Fig. 1. During the experiment, the samples were placed in a 2 mm inner diameter alumina tube. The experiment procedure includes first heating up the specimen gradually up to 750℃ and holding for 10 minutes to ensure fully temperature homogenization. Both the top and bottom heater was run at the same temperature hence, no temperature difference was applied to the specimen. The specimen was then cooled at a constant rate of 0.1℃/s until fully solidified.

Tomographic data processing

The collected tomograms were first reconstructed using the Savu package [42,43]. 3D anisotropic diffusion was applied to reduce the noise [44], followed by image segmentation in Avizo 9.2 (FEI VSG, France). To quantify the intermetallics, particle tracking and principal component analysis methods were used [31,45].

Deep etching and SEM characterization

Deep etching technique was used to reveal the 3D morphology of $Al_{13}Fe_4$ intermetallic by eliminating the aluminium matrix. 5% NaOH solution as an etchant was used to etch the sample for 1 hour. The sample used for deep etching was melted and cooled at a rate of 0.1 ℃/s in differential scanning calorimetry (NETZSCH DSC 404C). The microstructures of $Al_{13}Fe_4$ particles were characterised by a scanning electron microscopy (SEM-HITACHI TM3030 PLUS).

ToposPro and KrystalShaper

A unit cell of $Al_{13}Fe_4$ intermetallic was created from ToposPro [46] and KrystalShaper (JCrystalSoft, 2018) to demonstrate the crystal structure and shape.

3. Results and Discussion

3.1.Overall observation

High-speed synchrotron X-ray tomography allows the *in situ* observation of the solidification process of the $Al_{13}Fe_4$ intermetallic. A set of vertical slices are shown in Fig. 2a-2d, which illustrates the microstructure evolution in solidifying Al-5wt.%Fe alloy at *t*, *t*+40 s, *t*+100 s, *t*+400 s. (where *t* is the time when the first $Al_{13}Fe_4$ intermetallic appeared in the field of view). The $Al_{13}Fe_4$ intermetallics appeared to be much brighter than the aluminium liquid because the iron-rich intermetallics have higher X-ray attenuation than the liquid. This also allows the $Al_{13}Fe_4$ to be easily segmented from the aluminium liquid. Fig. 2e-2h represent the corresponding 3D rendered images of the intermetallics after image segmentation (see also the supplementary movie 1). The intermetallics are mostly plate-like shapes. The first

intermetallic was observed in Fig. 2-e, at $741 \pm 1℃$. This solidification starting temperature was determined from the binary Al-Fe phase diagram. Below this temperature, $Al_{13}Fe_4$ intermetallics continued to grow and new intermetallics nucleated rapidly. As shown in Fig. 2-f, after a fall in temperature of 4℃ from Fig. 2-e, many more intermetallics have nucleated. The number and size of intermetallics increase rapidly in the first 100 s to 731℃, as shown in Fig. 2-g. The formation of new intermetallics ceased at 701℃, with the total number of intermetallics formed being 62.

3.2.Nucleation of the intermetallic

In addition to the qualitative observation of the overall solidification behaviour of the Al-5wt%Fe alloy, we can also quantify the evolution of the $Al_{13}Fe_4$ intermetallics. Fig. 3a plots the volume fraction of $Al_{13}Fe_4$ intermetallic as a function of temperature from both experimental results and the Scheil solidification model. It shows that the experimentally determined values deviated from the Scheil model, indicating that the cooling profile may not be linear.

Fig. 3b shows a histogram of the nucleation density of the intermetallic (the number of nucleation sites divided by the volume of the sample) as a function of nucleation temperature. As discussed earlier, the first crystal nucleated at 741℃. The intermetallics mainly (more than 90%) nucleated in the temperature range from 741℃ to 724℃. The curve shows the nucleation density reaches its maximum at around 735℃, followed by a decline with the increasing of undercooling. A Gaussian distribution (Eq. 1) can be used to fit the nucleation density as a function of nucleation undercooling. The nucleation undercooling was approximated according to the difference between the predicted nucleation temperature and the observed nucleation temperature inferred from the tomography.

$$n = n_{max} \exp\left(-\frac{(\Delta T_N - \Delta T_M)^2}{{\Delta T_\sigma}^2}\right) \quad (1)$$

Where n is the nucleation density at a specific nucleation undercooling, ΔT_N is the nucleation undercooling. ΔT_M is the mean value of the Gaussian distribution of nucleation undercooling (6 ℃). ΔT_σ is the deviation of the Gaussian distribution (4.3℃). n_{max} is the maximum nucleation density ($0.73\ mm^{-3}$). The decline of the number of nucleation sites at a higher degree of nucleation undercooling can be explained by the solute depletion in the melt due to the growth of intermetallic particles.

The nucleation sites of the intermetallic can also be identified. In a prior study [19,47], it was found that Fe-rich intermetallics were promoted to nucleate at the surface of inclusion and the primary phase, as well as the outer oxide layer of the specimen. In this experiment, two different nucleation sites were identified. As shown in Fig. 4a-4b, most of the $Al_{13}Fe_4$ intermetallics connected to the sample surface (58 out of 62). The surface of the specimen is most likely covered with aluminium oxide [36]. The oxide layer exhibited high potency for the nucleation of $Al_{13}Fe_4$ phases. Another possibility is that the surface of the sample was first undercooled, which can then trigger heterogeneous nucleation of $Al_{13}Fe_4$ in the melt near the surface. The rapid growth of these $Al_{13}Fe_4$ crystals can release a significant amount of latent heat, which may

suppress nucleation in its nearby regions. Nucleation also occurred at the tip of existing intermetallics, as shown in Fig. 4-c1 to 4-c6 (Supplementary movie 2). Once nucleated, the crystal grew rapidly. In this case, the existing intermetallic can be considered as inclusions that provide high potential for nucleation.

3.3.Growth of the intermetallic

After nucleation, individual particles were tracked using a particle tracking method [31], allowing the quantification of individual intermetallic growth. Fig. 5-a shows the growth velocities of different particles as a function of the growth time. The growth velocities of impinged intermetallics are not included. The curves can be divided into two main types. The first type is that the particle growth rates increase at the initial stage of solidification (the first 50 seconds), then slow down slightly approaching constant values. The second type is that the particles have the highest growth rates initially, then the rates slowed down continuously as the temperature decreasing.

Fig. 5-b demonstrates the overall growth rate of intermetallics as a function of its nucleation time (t_n). t_n is the nucleation time of the particle n. As can be seen, the growth rates of most of the intermetallics are inversely proportional to the nucleation time. The first intermetallic has a growth rate of $3\times 10^4\ \mu m^3/s$. The overall growth rate dropped by 80% to 6000 $\mu m^3/s$ in 200 s. This might be because of the depletion of solutes which restricted the growth at the later stage of solidification [48].

The intermetallic was shown to grow into different faceted morphologies (Fig. 2). Here, four main shapes were observed, which are plate-like (Fig. 5-c1), stair-like (Fig. 5-c2), hexagonal tabular (Fig. 5-c3) and V-shaped (Fig. 5-c4). Fig. 5-c demonstrates the percentage of each morphology. Plate-like patterns have a frequency of 78%. Only a few intermetallics are classified into stair-like, hexagonal tabular and V-shaped structures in the percentage of 11%, 6% and 5%, respectively. The formation process of those different shape of crystals are discussed in the next section. The growth rate curves of the particles (Fig. 2-a) were coloured according to the morphologies. There seems to be no correlation between the growth velocities and the morphologies.

Morphologies and crystal structure

The melting entropy can be used to predict the crystallisation behaviour. The intermetallics that have high dimensionless entropy more than 2 (entropy of fusion ΔS_F =3.65) can form faceted phases [24]. Otherwise, they tend to form non-faceted structures. The entropy of fusion ΔS_F of $Al_{13}Fe_4$ is 4.6 [49]; hence the faceted structure was formed. The morphology of a crystal strongly relates to its crystal structure. The crystal structure of $Al_{13}Fe_4$ particles is monoclinic C2/m (a=1.549nm, b=0.808nm, c= 1.248nm, $\alpha=\gamma=90°$, $\beta=107.7°$) [25,50]. A unit cell and the simulated shape of the $Al_{13}Fe_4$ are shown in Fig. 6a to 6c. According to the crystal growth theory [51], the high-index planes have higher rates in accepting atoms and grow faster. These planes will disappear, and the crystal will be bounded by low-index planes that grow slowly. The low index planes of $Al_{13}Fe_4$ include (100), (001), $(20\bar{1})$ and (110). The

corresponding *d*-spacing and interplane angles are listed in Table 1. Previous studies have shown that the preferred extension direction of $Al_{13}Fe_4$ was suggested to be <010> or <011> [23]. The morphology evolution and growth rate quantification of each pattern from the four groups are demonstrated in Fig. 7-10.

The majority of the observed particles are plate-like. One example (number 1 marked in Fig.2) is shown in Fig. 7 a1-a6 at t_1, t_1+10 s, t_1+20 s, t_1+30 s, t_1+40 s, t_1+180 s (Supplementary movie 3), clearly showing the growth anisotropy. t_1 is the first time when the plate-like pattern appears in the selected field of view. the Fig. 7-b presents the evolution of the plate-like pattern in the first 40 seconds overlapped together. The first particle is in the shape of a thin plate in Fig. 7-a1. A series of re-entrant corners were formed along the edges of the plate, as pointed by the black arrows in Fig. 7-b. This repeated formation of re-entrant corners may contribute to the anisotropic growth and results in the plate-like intermetallics with high aspect ratios. This growth behaviour of $Al_{13}Fe_4$ was also observed by an in-situ radiographic observation [15].

Fig. 7-c1 and 7-c2 show the meshed intermetallics and the angles between different facets were measured. Fig. 7-c1 shows the front view of one plate-like crystal. All of the six proximal angles of this crystal are around 120°. According to Table 1, the angles between (100) and $(\bar{1}10)$ planes, between (110) and $(\bar{1}10)$ planes are both around 120°. This allows us to index the bounding facets to be (100), (110) and $(\bar{1}10)$ as shown in Fig. 7-c1. The extension direction of this crystal is <001> as shown in Fig. 7-c2. The simulated crystal shape (Fig. 6-b) bounded by those planes is similar to Fig. 7-c1.

We then used the principal component analysis [31,45] to calculate dimensions of the plate-like particles. The length, width and thickness of plate-shaped particles are the first, second and third principal component. Fig. 7-d1 presents the size evolution of one plate-like intermetallic in three directions as a function of temperature. Red, blue and black arrows indicate the measured direction of length, width and thickness, respectively. At t_1, the plate-like structure has 388 μm in length, 91 μm in width and 14 μm in thickness. It appears that the crystal grew rapidly at the early stage of crystallization especially at the length and width directions in the first 60 seconds. Then the growth rate slows down but continued to grow to 710 μm in length, 286 μm in width, and 49 μm in thickness in 180 s. This demonstrates the growth anisotropy of the $Al_{13}Fe_4$ crystal. It grew much faster in length and width than in thickness, which is most likely caused by the slow attachment of atoms on the flat faceted plane [52]. The quantified 3D dimensions of plate-like patterns can be used to verify the numerical modelling.

The average growth velocities of the plate-like intermetallics are presented in Fig. 7-d2. The average growth rate is the particle volume divided by its solidification time, while the instantaneous growth rate is the increased volume over 10 s divided by the interval (10 s). The selected plate-like particle has a growth rate of $1.4 \times 10^4\ \mathrm{um}^3/\mathrm{s}$ in the first 10 s, it then increased until a maximum value of $3.9 \times 10^4\ \mathrm{um}^3/\mathrm{s}$ in 60 s. Finally, it approached to a constant average growth rate around $3 \times 10^4\ \mathrm{um}^3/\mathrm{s}$ in 190 s.

Fig. 8-a presents the growth process of hexagonal tabular (number 2 marked in Fig.2) $Al_{13}Fe_4$ intermetallics (Supplementary movie 4). The intersection angles between the facets are different from the crystal in Fig. 7. Fig. 8-b shows the front view of the corresponding transparent images from Fig. 8-a, which provide a clear formation process of the crystal pattern. The first particle in Fig. 8-a1 has a hexagonal tabular shape rather than a thin plate as in Fig. 7-a. It first extended in y-direction towards liquid. It then coarsened in z-direction while the shape of the crystal was maintained. The crystal grew into a hexagon with almost equal edge length, different from the one in Fig. 7. The measured angles between facets are about 110° and 140°, as shown in Fig. 8-c1. According to Table 1, the angle between (100) and (001) planes is 107°, while the angle between (100) and $(20\bar{1})$ is 143°. Hence, we can index the bounding facets to be (100), (001) and $(20\bar{1})$ as shown in Fig. 8-c1. The extension direction for this crystal was subsequently identified to be <010>. The simulated crystal shape bounded by these planes is shown in Fig. 6-c, which closely resembles the shape of the hexagonal tabular crystal in Fig. 8-c. The volume change of the particle during growth was quantified as shown in Fig. 8-d1, the first pattern that was observed by tomography has the volume of $1.8 \times 10^5 \mu m^3$. After 150 seconds, the volume is increased to $10.8 \times 10^5 \mu m^3$. Fig. 8-d2 present the average growth velocities. The particle has the highest average growth rate of $1.8\ \mu m^3/s$ in the beginning, it then slowed down to a value of $0.7\ \mu m^3/s$. This growth behaviour may be due to slow atom attachment on all highly ordered faceted planes.

Another morphology is stair-like (number 3 marked in Fig.2), as shown in Fig. 9-a and 9-b (Supplementary movie 5). It can be seen that initially, a plate-like crystal form (Fig. 9-a_1 and a_2). Multiple re-entrants were also observed in Fig. 9-b. Later, part of the crystal on the flat surface started to thicken at a faster rate than the rest of the plate, forming a stair (Fig. 9-a_3 to a_6). Fig. 9-c1 and 9-c2 show the facets of the meshed stepped intermetallic. Similarly, we first measured the angles between different facets as shown in Fig. 9-c1. Then according to Table 1, we indexed the bounding planes. Stairs were frequently observed on the (001) facet of β-AlFeSi intermetallics in solidified Al-Si-Mg-Fe alloys, which were caused by the presences of lattice faults [52]. A similar mechanism can be used to explain the stair-like $Al_{13}Fe_4$ intermetallic formation: during $Al_{13}Fe_4$ growth, a fault could form on the (100) plane, resulting in low energy sites for atoms to deposit, forming a stair on top of the (100) facet. The volume of this pattern increased to $2.05 \times 10^6 \mu m^3$ in 110 s from $1.7 \times 10^5 \mu m^3$ in Fig. 9-d1. The quantification of the average growth velocities is presented in Fig. 9-d2. The average growth velocity increased from $1.7 \times 10^4\ \mu m^3/s$ to $2.5 \times 10^4\ \mu m^3/s$ in the first 40 s, it then reduced to $1.7 \times 10^4\ \mu m^3/s$.

The last morphology is V-shaped (number 4 marked in Fig.2) in Fig. 10-a and b, which have the lowest quantities (Supplementary movie 6). Only three intermetallics out of 62 were V-shaped. Fig. 10-c1 and 10-c2 show the front view and side view of a V-shaped particle. Li et al [23] observed a $Al_{13}Fe_4$ particle by SEM with similar

morphology (called as bended particle in their study), and suggested that it is a twinned particle. For $Al_{13}Fe_4$ crystal, (001) plane was proposed to be the possible twinning plane [15,23,53]. Here, the V-like structure can be considered as twins connected by two plate-like patterns which share a common plane. Here to identify and index the facets of the bended crystal, we also measured the angles between different facets, as shown in Fig. 10-c1. We started with two angles around $140°$ in Fig. 10-c1. Since the interplane angle between (100) and $(20\bar{1})$ is 143.9°, the bound facets of the angles were indexed to be (100) and $(20\bar{1})$. According to the shape of the crystal, we can identify a twinning plane marked by a red line. The measured angle between the red line and the top flat facet is about 109°. From Table 1, We know the angle between (100) and (001) is 107.7°. Hence, the twinning plane in the red line is highly likely to be (001) as suggested by Li et al [23],.

The growth mechanism of the V-shaped intermetallic is proposed to be as follows. First, an $Al_{13}Fe_4$ intermetallic was nucleated and grew into a small plate-like particle extending in <010> direction. This compound has a tendency to twin, and so a stacking fault relates to (001) plane may occur. The intermetallic was then extended in the reflected direction of the (001) twinning plane. Finally, the V-shaped intermetallic was bound by low index faces (100), (001) and $(20\bar{1})$.

The intermetallic grew to $6.18 \times 10^6 \mu m^3$ in 190s in Fig. 10-d1 continually. The average growth rate first increased then decreased. As shown in Fig. 10-d2, it has a growth velocity of $1.5 \times 10^4\ \mu m^3/s$ in the first 10 seconds, it then increased until a maximum value of $4.2 \times 10^4\ \mu m^3/s$ in 70 seconds. Finally, the average growth rate reduced to around $3 \times 10^4\ \mu m^3/s$.

3.4.Crystal-crystal interactions

Interactions between intermetallics during growth, mainly impingement, have also been observed, as depicted in Fig. 11-a to d (Supplementary movie 7). When two or more intermetallics grow towards each other, they will impinge and insert into one another. Before impingement (Fig. 11-a), the two crystals are both platelet-like. Fig. 11-b and 11-c show that the two crystals grew into each other at an angle. One of the crystals on the right-hand side, after impingement, became stair-like crystal (Fig. 11-c and 11-d), indicating that crystal-crystal interactions may alter the shape of the intermetallics, for instance, from plate-like to stairs. However, even faster tomographic scans are required to reveal this phenomenon in more detail.

3.5.Internal defect formation

An orthogonal cross-section slice extracted from the tomography shows internal defects (dark region, pointed by a red arrow) in the $Al_{13}Fe_4$ crystals (bright region) as displayed in Fig. 12-a. This kind of defects was also confirmed by SEM characterization (Fig. 12-b). Fig. 12-c and 12-d show the morphology of the internal defects in 3D (red coloured), which were connected to the crystal surface and appears to be hole-like. The shape of

the crystal was rendered as transparent. The hole-like defects were not porosities but filled with aluminium melt since they have the same image contrast as the melt. Fig. 12-e to fig. 12-h demonstrate the surface morphology of a crystal with internal defects in 3D at t_6+30 s, t_6+90 s, t_6+160 s and t_6+560 s (Supplementary movie 8). At the early stage of crystal formation, some irregularities appeared on the supposedly flat surface, which became grooves as shown in Fig. 12-f. The grooves appear to be engulfed later on during solidification, leading to the formation of internal defects/holes. The process was schematically shown in Fig. 12-i. Similar defects or holes in faceted Ge crystals were also observed by Shahani et al.,[54] in Al-Ge alloys, and their formation was attributed twinning and plate branching. The surface defects of faceted Al_5FeSi intermetallics observed in Al-Si alloys [19] was attributed to the physical interaction of the intermetallics with aluminium dendrites.

3.6.Potential Growth hypothesis

Fig. 13-a and 13-b reveal the SEM images of deeply etched $Al_{13}Fe_4$ particles. During the etching process, aluminium acts as an anode, and the $Al_{13}Fe_4$ particles act as a cathode [55]. After deep etching, the aluminium matrix surrounding the iron intermetallics were dissolved, revealing $Al_{13}Fe_4$ blocks. The hexagonal tabular (Fig.13-a) and plate-shaped particles (Fig.13-b) were observed. There are also many cracks on the surface of the deep-etched particles and a large hole, although we cannot confirm whether the cracks and hole were formed during crystal growth or as a result of deep-etching. On the side facets, the cracks seem to be organized (pointed by red arrows), dividing the crystal facets into many sub-units.

Here, we propose a hypothesis that the growth behaviour of $Al_{13}Fe_4$ intermetallic may be the oriented particle attachment [56]. There also have more widespread acceptance that crystals form through the assembly of building subunits/blocks [57,58], an alternative pathway for crystallisation. During the nucleation stage, precursors nucleated and grew into small crystal subunits (Fig. 13 c-t1). As the temperature lowering, new subunits could form in the nearby region and attached together to form a large crystal then this large one will coarsen as more subunits are attached (Fig. 13 c-t2 and t3). Some faults might form during this process, leading to a change of the attaching order and the formation of internal defects (Fig. 13 c- t4) and various shapes (Fig. 13-d and 13-e). Similar mechanisms were proposed to describe the formation of faceted Al_2Cu intermetallics in Al-Cu alloy [59]. However, we do not have direct evidence to confirm this hypothesis in this study except that the SEM images (Fig. 13-a and 13-b) of deep etched samples shows that the crystals are cracked into regular subunits. A recent study by *in situ* X-ray radiography shows that the growth of $Al_{13}Fe_4$ is by repeated attachment of $Al_{13}Fe_4$ sub-platelets to its corners [15], which could be understood as oriented particle attachment. To prove or disprove this hypothesis, we need to carry out extensively more research, including (1) nano-scale *in situ* TEM [60] or X-ray tomography [61] to observe the nucleation process of intermetallics which the aim to identify the subunits; and (2) even fast micro-scale tomography (sub-second) [62] to visualize the crystallization process.

4. Conclusion

In summary, the formation of $Al_{13}Fe_4$ intermetallic in a solidifying Al-5wt% Fe alloy was quantified via 4D synchrotron X-ray imaging. The *in situ* solidification under a slow cooling rate ($0.1℃/s$) was performed at scan intervals of 10 s, which allows us to observe the rapid nucleation and growth of faceted $Al_{13}Fe_4$ intermetallic. The work demonstrates that high-speed synchrotron X-ray tomography can be a useful tool to reveal the dynamic of faceted crystal growth. The following conclusions can be made:

1. Regarding the nucleation of $Al_{13}Fe_4$, the intermetallics (more than 95%) prevalently nucleated near the melt surface and the rest nucleated on the intermetallics formed earlier. The number of nucleation sites or nucleation density as a function of the temperature follows a Gaussian distribution, providing a sufficient equation for numerical modelling of intermetallic growth.
2. Individually faceted intermetallics were classified and quantitated. Four types of intermetallics were found based on different morphologies, which are plate-like, hexagonal tabular , stair-like and V-shaped. The variation in morphologies was explained by the crystal structure and twinning of the particle. Both volume change and growth velocity of the formation processes were provided.
3. The processes by which hole-like defects form, on the surface and inside the faceted $Al_{13}Fe_4$ intermetallic, were observed.
4. A potential hypothesis of oriented particle attachment was proposed to describe the faceted crystal growth and internal defect formation. However, even faster tomography with higher resolution is required to observe the attachment process in solidifying $Al_{13}Fe_4$ intermetallics.

Acknowledgements

The authors acknowledge the I12 beamline, Diamond light source, Oxford for providing the beamtime EE19216-1 and technique support. Z. Song thanks the UK-EPSRC CDT Grant (No: EP/L016206/1) in Innovative Metal Processing for financial support. B.C. acknowledges the funding supported from the Diamond Birmingham Collaboration and the Alan Turing Fellowship.

References:

[1] T. Wang, P. Zhou, F. Cao, H. Kang, Z. Chen, Y. Fu, T. Xiao, W. Huang, Q. Yuan, Growth behavior of Cu6Sn5 in Sn-6.5 Cu solders under DC considering trace Al: In situ observation, Intermetallics. 58 (2015) 84–90. https://doi.org/10.1016/j.intermet.2014.11.010.

[2] S.-H. Kim, H. Kim, N.J. Kim, Brittle intermetallic compound makes ultrastrong low-density steel with large ductility, Nature. 518 (2015) 77–79. https://doi.org/10.1038/nature14144.

[3] K. Tran, Z.W. Ulissi, Active learning across intermetallics to guide discovery of electrocatalysts for CO2 reduction and H2 evolution, Nat. Catal. 1 (2018) 696–703. https://doi.org/10.1038/s41929-018-0142-1.

[4] Y. Liu, W. Liu, Y. Ma, C. Liang, C. Liu, C. Zhang, Q. Cai, Microstructure and wear resistance of compositionally graded Ti–Al intermetallic coating on Ti6Al4V alloy fabricated by laser powder deposition, Surf. Coatings Technol. 353 (2018) 32–40. https://doi.org/10.1016/j.surfcoat.2018.08.067.

[5] K. Gschneidner, A. Russell, A. Pecharsky, J. Morris, Z. Zhang, T. Lograsso, D. Hsu, C.H.C. Lo, Y. Ye, A. Slager, D. Kesse, A family of ductile intermetallic compounds, Nat. Mater. 2 (2003) 587–590. https://doi.org/10.1038/nmat958.

[6] A.J. Shahani, X. Xiao, K. Skinner, M. Peters, P.W. Voorhees, Ostwald ripening of faceted Si particles in an Al-Si-Cu melt, Mater. Sci. Eng. A. 673 (2016) 307–320. https://doi.org/10.1016/j.msea.2016.06.077.

[7] M.R.J. Scherer, P.M.S. Cunha, U. Steiner, Labyrinth-induced faceted electrochemical growth, Adv. Mater. 26 (2014) 2403–2407. https://doi.org/10.1002/adma.201305074.

[8] K.G. Libbrecht, Physical Dynamics of Ice Crystal Growth, Annu. Rev. Mater. Res. 47 (2017) 271–295. https://doi.org/10.1146/annurev-matsci-070616-124135.

[9] J.W. Barrett, H. Garcke, R. Nürnberg, Numerical computations of faceted pattern formation in snow crystal growth, Phys. Rev. E - Stat. Nonlinear, Soft Matter Phys. 86 (2012) 4–8. https://doi.org/10.1103/PhysRevE.86.011604.

[10] M. Polacci, F. Arzilli, G. La Spina, N. Le Gall, B. Cai, M.E. Hartley, D. Di Genova, N.T. Vo, S. Nonni, R.C. Atwood, E.W. Llewellin, P.D. Lee, M.R. Burton, Crystallisation in basaltic magmas revealed via in situ 4D synchrotron X-ray microtomography, Sci. Rep. 8 (2018) 1–13. https://doi.org/10.1038/s41598-018-26644-6.

[11] E. Taghaddos, M.M. Hejazi, R. Taghiabadi, S.G. Shabestari, Effect of iron-intermetallics on the fluidity of 413 aluminum alloy, J. Alloys Compd. 468 (2009) 539–545. https://doi.org/10.1016/j.jallcom.2008.01.079.

[12] D. Liang, H. Jones, Morphologies of primary Al3Fe in Bridgman solidification and TIG weld traversing of hypereutectic AlFe alloys, Mater. Sci. Eng. A. 173 (1993) 109–114. https://doi.org/10.1016/0921-5093(93)90197-M.

[13] H. Kang, T. Wang, X. Li, Y. Su, J. Guo, H. Fu, Faceted-nonfaceted growth

transition and 3-D morphological evolution of primary Al6Mn microcrystals in directionally solidified Al-3 at.% Mn alloy, J. Mater. Res. 29 (2014) 1256–1263. https://doi.org/10.1557/jmr.2014.111.

[14] S. Hu, A. Gagnoud, Y. Fautrelle, R. Moreau, X. Li, Fabrication of aluminum alloy functionally graded material using directional solidification under an axial static magnetic field, Sci. Rep. 8 (2018) 1–13. https://doi.org/10.1038/s41598-018-26297-5.

[15] S. Feng, Y. Cui, E. Liotti, A. Lui, C.M. Gourlay, P.S. Grant, In-situ X-ray radiography of twinned crystal growth of primary Al13Fe4, Scr. Mater. 184 (2020) 57–62. https://doi.org/10.1016/j.scriptamat.2020.04.010.

[16] Z. Ma, A.M. Samuel, F.H. Samuel, H.W. Doty, S. Valtierra, A study of tensile properties in Al-Si-Cu and Al-Si-Mg alloys: Effect of β-iron intermetallics and porosity, Mater. Sci. Eng. A. 490 (2008) 36–51. https://doi.org/10.1016/j.msea.2008.01.028.

[17] S.G. Shabestari, E. Parshizfard, Effect of semi-solid forming on the microstructure and mechanical properties of the iron containing Al-Si alloys, J. Alloys Compd. 509 (2011) 7973–7978. https://doi.org/10.1016/j.jallcom.2011.05.052.

[18] J. Hirsch, T. Al-Samman, Superior light metals by texture engineering: Optimized aluminum and magnesium alloys for automotive applications, Acta Mater. 61 (2013) 818–843. https://doi.org/10.1016/j.actamat.2012.10.044.

[19] S. Terzi, J.A. Taylor, Y.H. Cho, L. Salvo, M. Suéry, E. Boller, A.K. Dahle, In situ study of nucleation and growth of the irregular α-Al/β-Al5FeSi eutectic by 3-D synchrotron X-ray microtomography, Acta Mater. 58 (2010) 5370–5380. https://doi.org/10.1016/j.actamat.2010.06.012.

[20] X. Wu, H. Zhang, F. Zhang, Z. Ma, L. Jia, B. Yang, T. Tao, H. Zhang, Effect of cooling rate and Co content on the formation of Fe-rich intermetallics in hypoeutectic Al7Si0.3Mg alloy with 0.5%Fe, Mater. Charact. 139 (2018) 116–124. https://doi.org/10.1016/j.matchar.2018.02.029.

[21] Y. Han, C. Ban, H. Zhang, H. Nagaumi, Q. Ba, J. Cui, Investigations on the Solidification Behavior of Al-Fe-Si Alloy in an Alternating Magnetic Field, Mater. Trans. 47 (2006) 2092–2098. https://doi.org/10.2320/matertrans.47.2092.

[22] Y. Han, C. Ban, S. Guo, X. Liu, Q. Ba, J. Cui, Alignment behavior of primary Al3Fe phase in Al-Fe alloy under a high magnetic field, Mater. Lett. 61 (2007) 983–986. https://doi.org/10.1016/j.matlet.2006.06.027.

[23] L. Li, Y. Zhang, C. Esling, H. Jiang, Z. Zhao, Y. Zuo, J. Cui, Crystallographic features of the primary Al3Fe phase in as-cast Al-3.31wt% Fe alloy, J. Appl. Crystallogr. 43 (2010) 1108–1112. https://doi.org/10.1107/S0021889810029493.

[24] A.J. McLeod, L.M. Hogan, C.M. Adam, D.C. Jenkinson, Growth mode of the aluminum phase in Al-Si and Al-Al3Fe eutectics, J. Cryst. Growth. 19 (1973) 301–309. https://doi.org/10.1016/0022-0248(73)90054-7.

[25] P. Skjerpe, An electron microscopy study of the phase Al3Fe, J. Microsc. 148 (1987) 33–50. https://doi.org/10.1111/j.1365-2818.1987.tb02853.x.

[26] G. Zeng, J.W. Xian, C.M. Gourlay, Nucleation and growth crystallography of Al8Mn5 on B2-Al(Mn,Fe) in AZ91 magnesium alloys, Acta Mater. 153 (2018) 364–376. https://doi.org/10.1016/j.actamat.2018.04.032.

[27] A. Bjurenstedt, D. Casari, S. Seifeddine, R.H. Mathiesen, A.K. Dahle, In-situ study of morphology and growth of primary α-Al(FeMnCr)Si intermetallics in an Al-Si alloy, Acta Mater. 130 (2017) 1–9. https://doi.org/10.1016/j.actamat.2017.03.026.

[28] B. Kim, S. Lee, H. Yasuda, Morphological Variation of Fe/Cr-Rich Intermetallic Phase in Recycled Al-Si Alloy as a Function of Solidification Rate: Time-Resolved Radiography, Mater. Sci. Forum - MATER SCI FORUM. 654 (2010) 974–977. https://doi.org/10.4028/www.scientific.net/MSF.654-656.974.

[29] J. Wang, P.D. Lee, R.W. Hamilton, M. Li, J. Allison, The kinetics of Fe-rich intermetallic formation in aluminium alloys: In situ observation, Scr. Mater. 60 (2009) 516–519. https://doi.org/10.1016/j.scriptamat.2008.11.048.

[30] T. Nelson, B. Cai, N. Warnken, P.D. Lee, E. Boller, O. V. Magdysyuk, N.R. Green, Gravity effect on thermal-solutal convection during solidification revealed by four-dimensional synchrotron imaging with compositional mapping, Scr. Mater. 180 (2020) 29–33. https://doi.org/10.1016/j.scriptamat.2019.12.026.

[31] B. Cai, A. Kao, P.D. Lee, E. Boller, H. Basevi, A.B. Phillion, A. Leonardis, K. Pericieous, Growth of β intermetallic in an Al-Cu-Si alloy during directional solidification via machine learned 4D quantification, Scr. Mater. 165 (2019) 29–33. https://doi.org/10.1016/j.scriptamat.2019.02.007.

[32] B. Cai, J. Wang, A. Kao, K. Pericleous, A.B. Phillion, R.C. Atwood, P.D. Lee, 4D synchrotron X-ray tomographic quantification of the transition from cellular to dendrite growth during directional solidification, Acta Mater. 117 (2016) 160–169. https://doi.org/10.1016/j.actamat.2016.07.002.

[33] J.M. Yu, N. Wanderka, A. Rack, R. Daudin, E. Boller, H. Markötter, A. Manzoni, F. Vogel, T. Arlt, I. Manke, J. Banhart, Formation of intermetallic δ phase in Al-10Si-0.3Fe alloy investigated by in-situ 4D X-ray synchrotron tomography, Acta Mater. 129 (2017) 194–202. https://doi.org/10.1016/j.actamat.2017.02.048.

[34] A.J. Shahani, E.B. Gulsoy, S.O. Poulsen, X. Xiao, P.W. Voorhees, Twin-mediated crystal growth: An enigma resolved, Sci. Rep. 6 (2016) 1–11. https://doi.org/10.1038/srep28651.

[35] J.W. Gibbs, P.W. Voorhees, Segmentation of four-dimensional, X-ray computed tomography data, Integr. Mater. Manuf. Innov. 3 (2014) 73–84. https://doi.org/10.1186/2193-9772-3-6.

[36] C. Puncreobutr, A.B. Phillion, J.L. Fife, P. Rockett, A.P. Horsfield, P.D. Lee, In situ quantification of the nucleation and growth of Fe-rich intermetallics

during Al alloy solidification, Acta Mater. 79 (2014) 292–303. https://doi.org/10.1016/j.actamat.2014.07.018.

[37] M. Wang, W. Xu, Q. Han, Study of Refinement and Morphology Change of AlFeSi Phase in A380 Alloy due to Addition of Ca, Sr/ Ca, Mn and Mn, Sr, Mater. Trans. 57 (2016) 1509–1513. https://doi.org/10.2320/matertrans.m2015329.

[38] M. Drakopoulos, T. Connolley, C. Reinhard, R. Atwood, O. Magdysyuk, N. Vo, M. Hart, L. Connor, B. Humphreys, G. Howell, S. Davies, T. Hill, G. Wilkin, U. Pedersen, A. Foster, N. De Maio, M. Basham, F. Yuan, K. Wanelik, I12: The Joint Engineering, Environment and Processing (JEEP) beamline at Diamond Light Source, J. Synchrotron Radiat. 22 (2015) 828–838. https://doi.org/10.1107/S1600577515003513.

[39] Y. Zhao, W. Du, B. Koe, T. Connolley, S. Irvine, P.K. Allan, C.M. Schlepütz, W. Zhang, F. Wang, D.G. Eskin, J. Mi, 3D characterisation of the Fe-rich intermetallic phases in recycled Al alloys by synchrotron X-ray microtomography and skeletonisation, Scr. Mater. 146 (2018) 321–326. https://doi.org/10.1016/j.scriptamat.2017.12.010.

[40] K. Yamagiwa, Y. Watanabe, Y. Fukui, P. Kapranos, Novel Recycling System of Aluminum and Iron Wastes- in-situ Al-Al 3 Fe Functionally Graded Material Manufactured by a Centrifugal Method-, Mater. Trans. 44 (2003) 2461–2467.

[41] K. Yamagiwa, Y. Watanabe, K. Matsuda, Y. Fukui, P. Kapranos, Characteristics of a near-net-shape formed Al-Al3Fe eco-functionally graded material produced over its eutectic melting temperature, Mater. Sci. Eng. A. 416 (2006) 80–91. https://doi.org/10.1016/j.msea.2005.10.031.

[42] F. Marone, M. Stampanoni, Regridding reconstruction algorithm for real-time tomographic imaging, J. Synchrotron Radiat. 19 (2012) 1029–1037. https://doi.org/10.1107/S0909049512032864.

[43] R.C. Atwood, A.J. Bodey, S.T. Price, M. Basham, M. Drakopoulos, A high-throughput system for high-quality tomographic reconstruction of large datasets at Diamond Light Source, Philos. Trans. R. Soc. A Math. Phys. Eng. Sci. (2015). https://doi.org/10.1098/rsta.2014.0398.

[44] E. Guo, A.B. Phillion, B. Cai, S. Shuai, D. Kazantsev, T. Jing, P.D. Lee, Dendritic evolution during coarsening of Mg-Zn alloys via 4D synchrotron tomography, Acta Mater. 123 (2017) 373–382. https://doi.org/10.1016/j.actamat.2016.10.022.

[45] S. Yue, P.D. Lee, G. Poologasundarampillai, J.R. Jones, Evaluation of 3-D bioactive glass scaffolds dissolution in a perfusion flow system with X-ray microtomography, Acta Biomater. 7 (2011) 2637–2643. https://doi.org/10.1016/j.actbio.2011.02.009.

[46] V.A. Blatov, A.P. Shevchenko, D.M. Proserpio, Applied topological analysis of crystal structures with the program package topospro, Cryst. Growth Des. 14 (2014) 3576–3586. https://doi.org/10.1021/cg500498k.

[47] W. Khalifa, F.H. Samuel, J.E. Gruzleski, H.W. Doty, S. Valtierra, Nucleation of Fe-Intermetallic Phases in the Al-Si-Fe Alloys, Metall. Mater. Trans. A. 36 (2005) 1017–1032.

[48] Z. Fan, F. Gao, L. Zhou, S.Z. Lu, A new concept for growth restriction during solidification, Acta Mater. 152 (2018) 248–257. https://doi.org/10.1016/j.actamat.2018.04.045.

[49] C.M.L. Adam, L.M. Hogan, Crystallography of the Al-Al3Fe eutectic, Acta Metall. 23 (1975) 345–354. https://doi.org/10.1016/0001-6160(75)90127-3.

[50] P.J. Black, The structure of $FeAl_3$. I, Acta Crystallogr. 8 (1955) 43–48. https://doi.org/10.1107/S0365110X5500011X.

[51] W. Kurz, D.J. Fisher, Fundamentals of Solidification, 4th rev. e, 1992.

[52] G. Sha, K.A.Q. O'Reilly, B. Cantor, Characterization of fe-rich intermetallic phases in a 6xxx series al alloy, Mater. Sci. Forum. 519–521 (2006) 1721–1726. https://doi.org/10.4028/www.scientific.net/msf.519-521.1721.

[53] M. Ellner, U. Burkhardt, Zur bildung von drehmehrlingen mit pentagonaler pseudosymmetrie beim erstarrungsvorgang des Fe4Al13, J. Alloys Compd. 198 (1993) 91–100. https://doi.org/10.1016/0925-8388(93)90150-L.

[54] A.J. Shahani, X. Xiao, P.W. Voorhees, The mechanism of eutectic growth in highly anisotropic materials, Nat. Commun. 7 (2016) 1–7. https://doi.org/10.1038/ncomms12953.

[55] K.S. Eom, J.Y. Kwon, M.J. Kim, H.S. Kwon, Design of Al-Fe alloys for fast on-board hydrogen production from hydrolysis, J. Mater. Chem. 21 (2011) 13047–13051. https://doi.org/10.1039/c1jm11329a.

[56] V.K. Ivanov, P.P. Fedorov, A.Y. Baranchikov, V. V Osiko, Oriented attachment of particles: 100 years of investigations of non-classical crystal growth, Russ. Chem. Rev. 1204 (2014) 127–131. https://doi.org/10.1016/b978-0-08-012210-6.50078-8.

[57] G. Mirabello, A. Ianiro, P.H.H. Bomans, T. Yoda, A. Arakaki, H. Friedrich, G. de With, N.A.J.M. Sommerdijk, Crystallization by particle attachment is a colloidal assembly process, Nat. Mater. 19 (2019) 391–396. https://doi.org/10.1038/s41563-019-0511-4.

[58] A.I. Lupulescu, J.D. Rimer, In situ imaging of silicalite-1 surface growth reveals the mechanism of crystallization, Science (80-.). 344 (2014) 729–732. https://doi.org/10.1126/science.1250984.

[59] K. Gao, S. Li, L. Xu, H. Fu, Effect of sample size on intermetallic Al2Cu microstructure and orientation evolution during directional solidification, J. Cryst. Growth. 394 (2014) 89–96. https://doi.org/10.1016/j.jcrysgro.2014.02.023.

[60] M.H. Nielsen, S. Aloni, J.J. De Yoreo, In situ TEM imaging of CaCO3 nucleation reveals coexistence of direct and indirect pathways, Science (80-.). 345 (2014) 1158–1162. https://doi.org/10.1126/science.1254051.

[61] R. Kumar, J. Villanova, P. Lhuissier, L. Salvo, In situ nanotomography study of creep cavities in Al-3.6-Cu alloy, Acta Mater. 166 (2019) 18–27. https://doi.org/10.1016/j.actamat.2018.12.020.

[62] R. Daudin, S. Terzi, P. Lhuissier, J. Tamayo, M. Scheel, N.H. Babu, D.G. Eskin, L. Salvo, Particle-induced morphological modification of Al alloy equiaxed dendrites revealed by sub-second in situ microtomography, Acta Mater. 125 (2017) 303–310. https://doi.org/10.1016/j.actamat.2016.12.005.

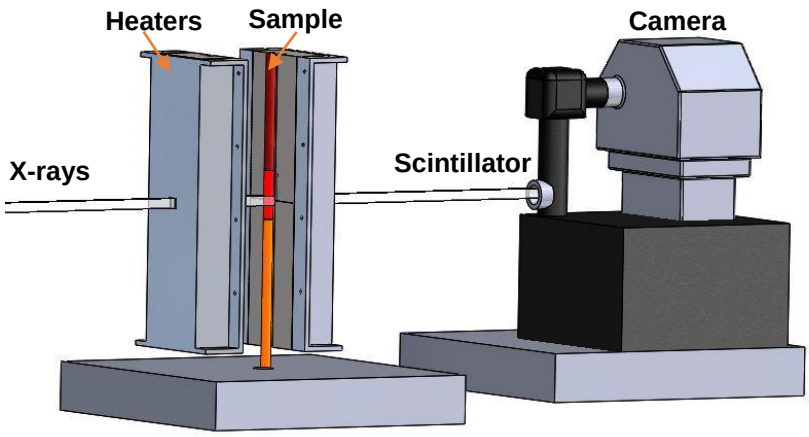

Fig. 1. Schematic of the experiment apparatus

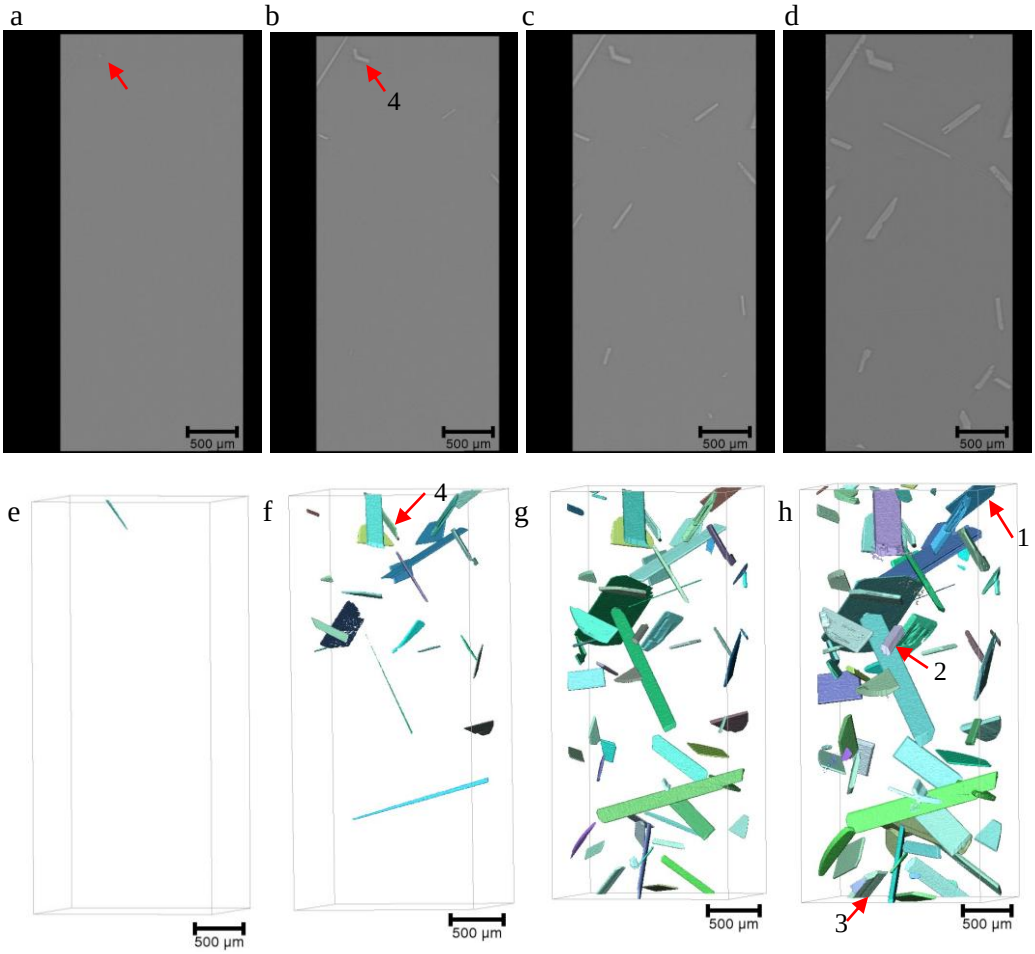

Fig. 2. (a-d) 2D slices extracted from the tomography at t, t+40 s, t+100 s, t+400 s; (e-h) 3D rendered volume of intermetallic at t ,t+40 s,t+100 s,t+400 s; numbers 1-4 indicate four morphologies: plate-like (1), hexagonal tabular (2), stair-like (3) and V-shaped (4).

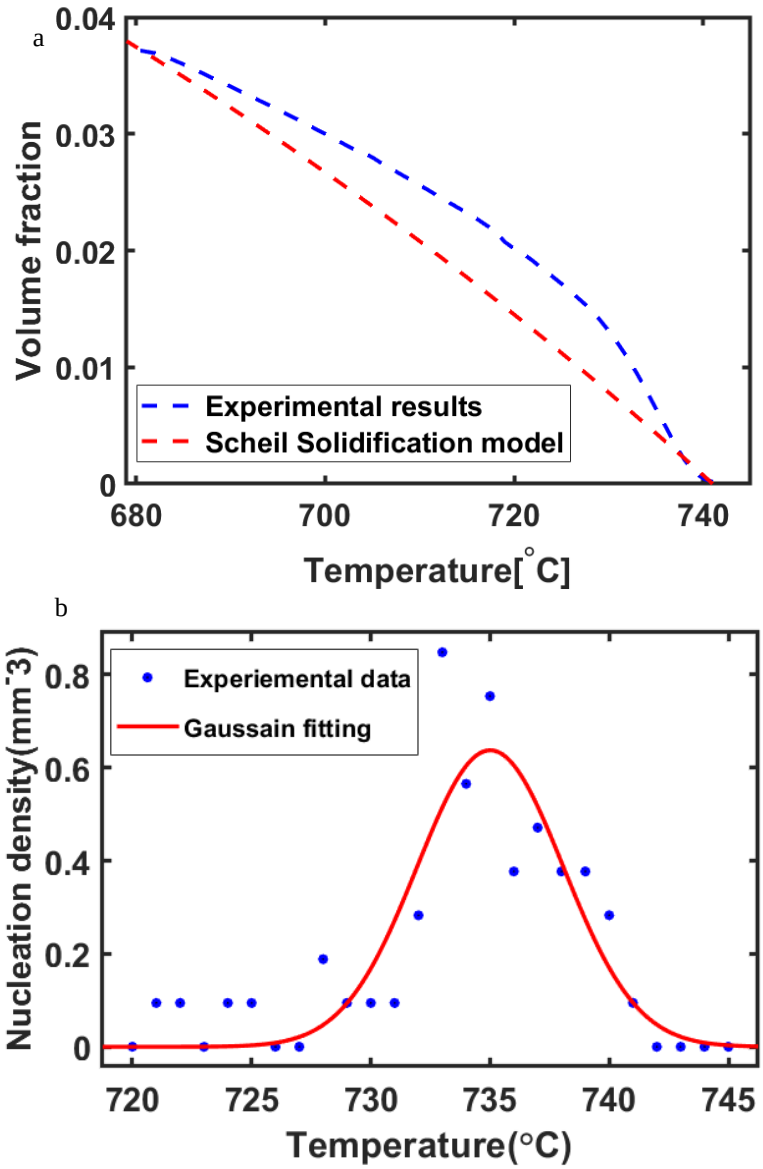

Fig. 3. (a)Volume fraction; (b) nucleation density as a function of temperature.

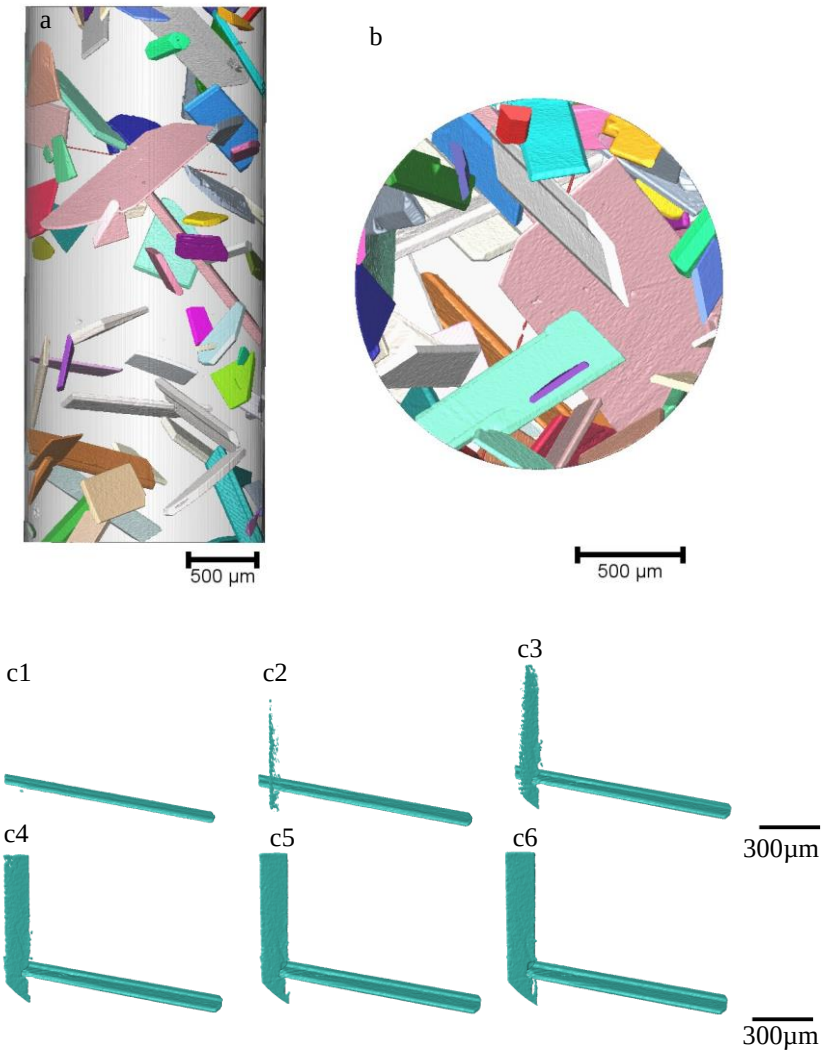

Fig. 4. 3D rendered intermetallics to show the nucleation on oxide surface (a) side view and (b) top view; (c1-c6) self-nucleation at t_0 +20 s to t_0 +70 s.

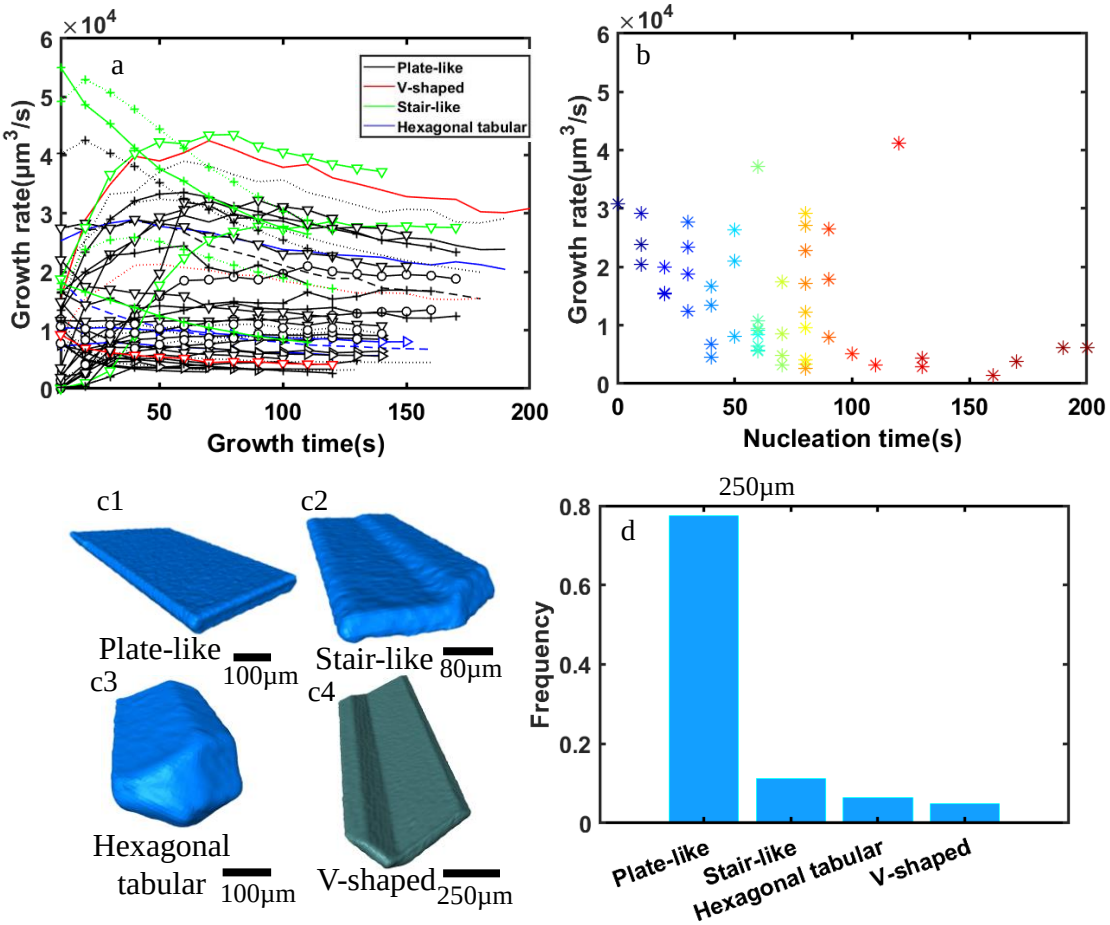

Fig. 5. (a) Growth rates of intermetallics from t to t+200 s; (b) Overall growth rate of intermetallics as a function of its nucleation time;(c1-c4) Selected intermetallics from each morphology category; (d) Frequency of various morphologies.

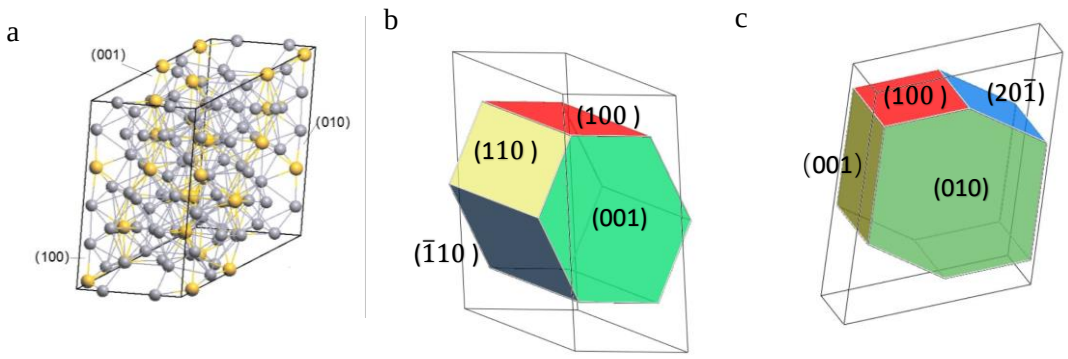

Fig. 6 (a) Unit cell; (b) simulated planes of the plate-like $Al_{13}Fe_4$ intermetallic; (c) simulated planes of the hexagonal tabular $Al_{13}Fe_4$ intermetallic.

Table 1: d-spacing and interplane angles of $Al_{13}Fe_4$ intermetallic

Planes	(001)	$(20\bar{1})$	(110)	$(\bar{1}10)$	**d-spacing(nm)**
(100)	107.69°	143.89°	118.7°	-	1.476
(001)	-	108.42°	98.39°	-	1.188
$(20\bar{1})$	-	-	112.82°	-	0.735
(110)	-	-	-	122.62°	0.709

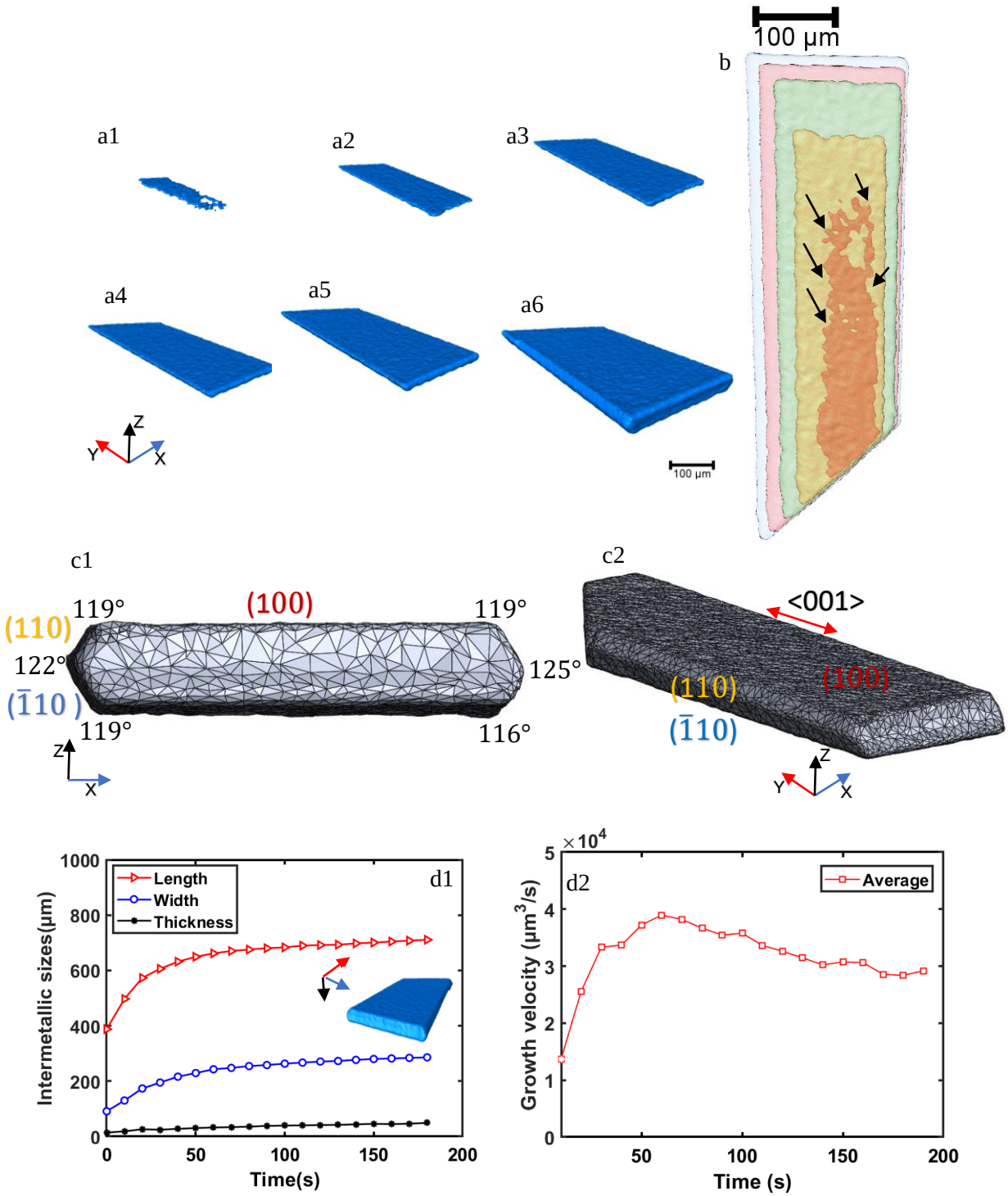

Fig. 7. (a1-a4) 3D rendered volume of plate-like $Al_{13}Fe_4$ at t_1, t_1+10 s, t_1+20 s, t_1+30 s, t_1+ 40 s , t_1+180 s; (b) Transparent image of plate-like $Al_{13}Fe_4$ at t_1, t_1+10 s, t_1+20 s, t_1+30 s, t_1+ 40 s; (c) Meshed plate-like intermetallic and the angles between different facets; (d1) Growth of plate-like particle in three dimensions; (d2) Growth velocity of the plate-like particle.

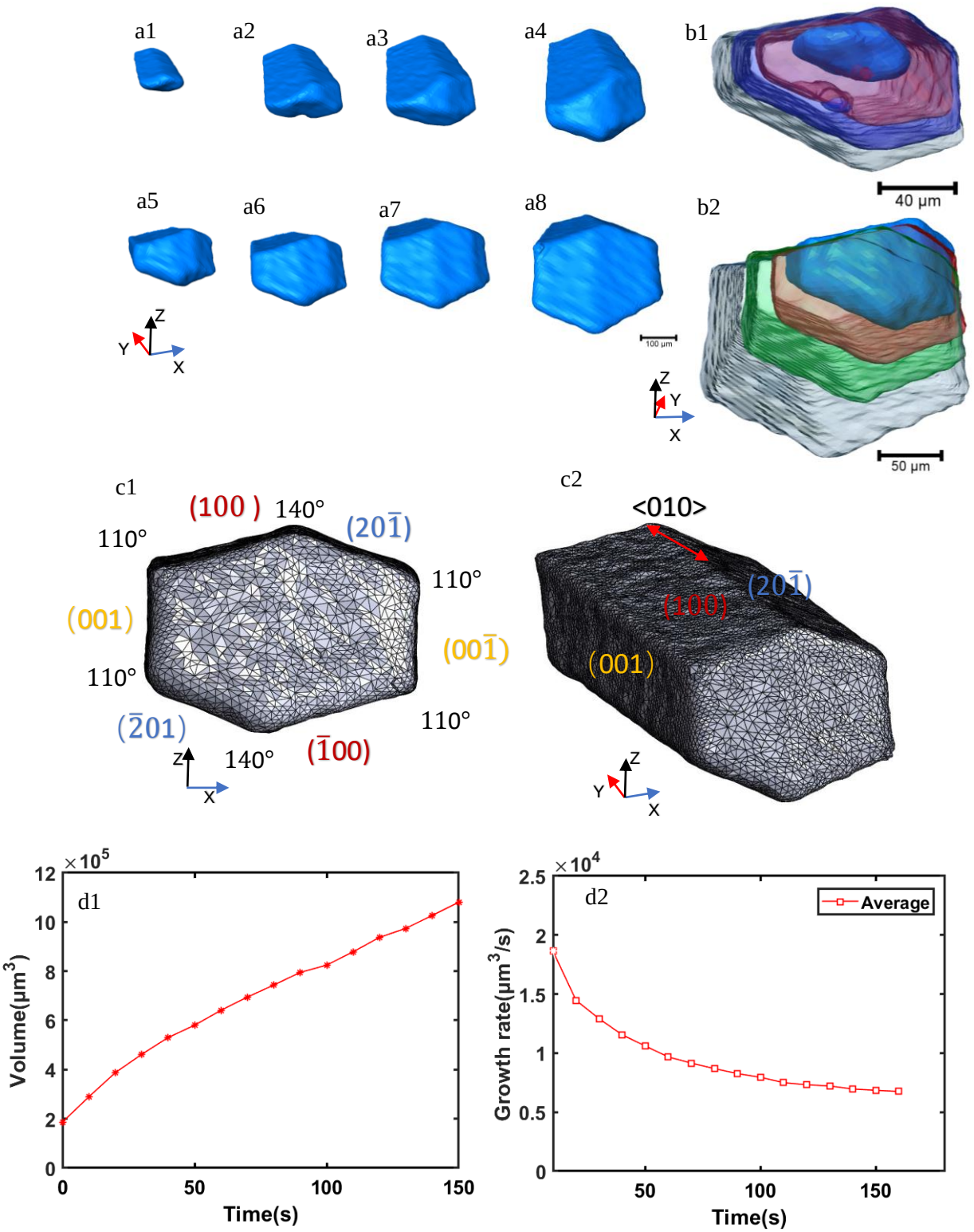

Fig. 8. (a1-a8) 3D rendered volume of hexagonal tabular $Al_{13}Fe_4$ at t_2, t_2+60 s, t_2+110 s, t_2+160 s, t_2+220 s, t_2+ 330 s , t_2+ 440 s t_2+610 s; (b) Transparent images (c) Meshed hexagonal tabular intermetallic and the angles between different facets; (d1)Volume change of the particle as a function of time (d2) Growth velocity of the hexagonal tabular particle.

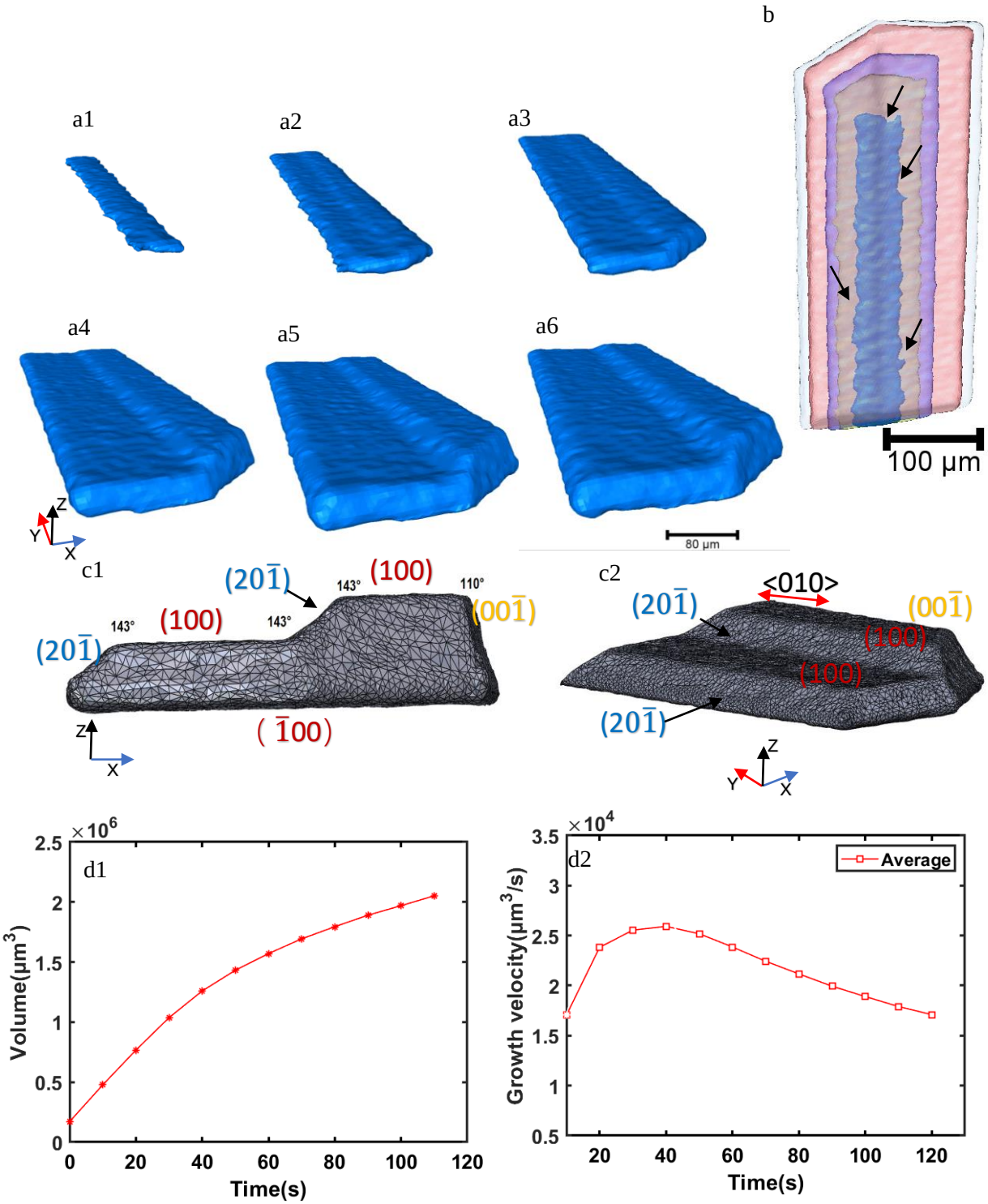

Fig. 9. (a) 3D rendered volume of stair-like $Al_{13}Fe_4$ at t_3, t_3+10 s, t_3+20 s, t_3+60 s, t_3+100 s , t_3+110 s; (b) Transparent image of stair-like $Al_{13}Fe_4$ t_3, t_3+10 s, t_3+20 s, t_3+ 100 s , t_3+110 s; (c) Meshed stair-like intermetallic and the angles between different facets; (d1)Volume change of the stair-like particle as a function of time (d2) Growth velocity of the stair-like particle.

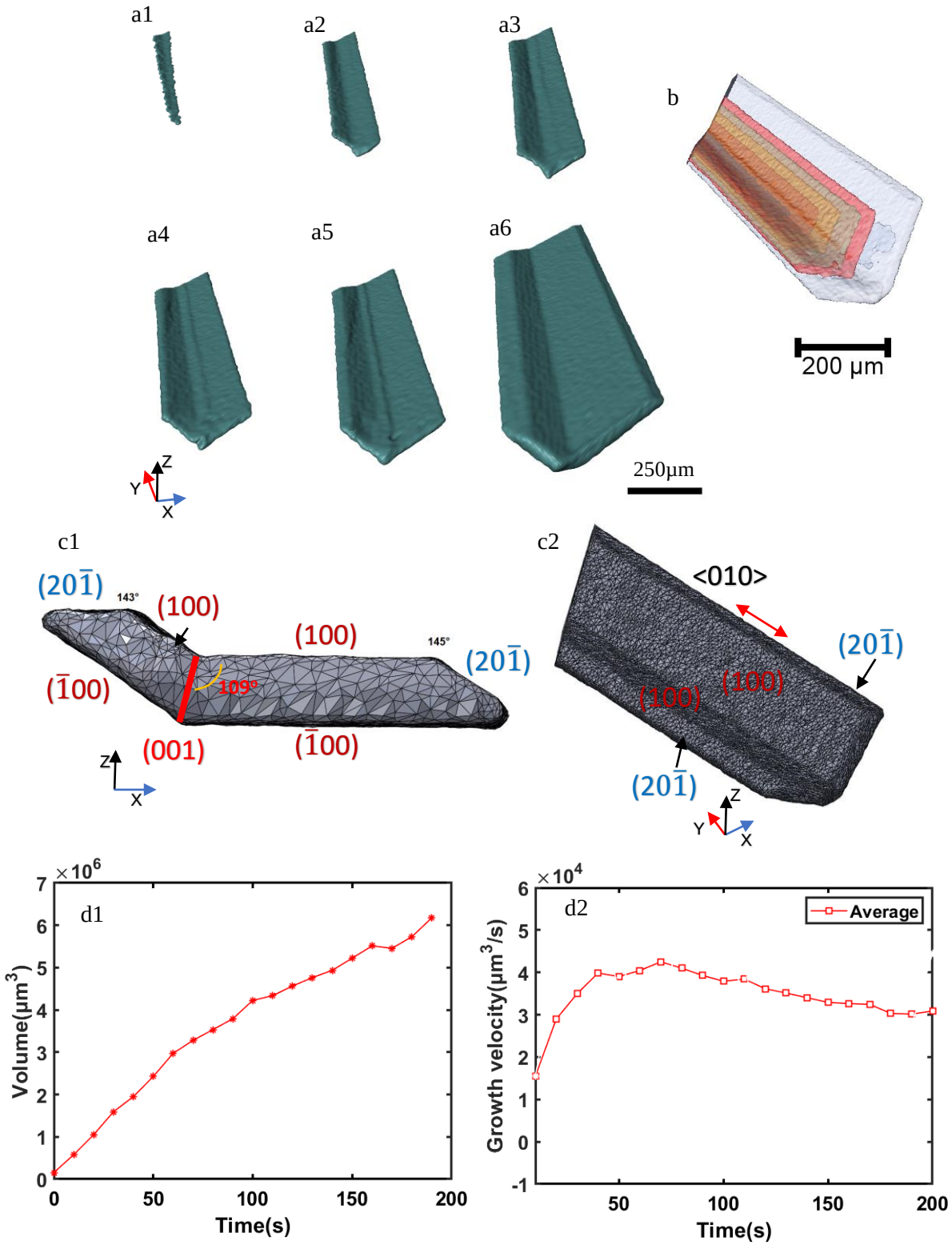

Fig. 10. (a) 3D rendered volume of V-shaped $Al_{13}Fe_4$ at t_4, t_4+10 s, t_4+20 s, t_4+30 s, t_4+40 s , t_4+190 s; (b) Transparent image of V-shaped $Al_{13}Fe_4$ t_4, t_4+10 s, t_4+20 s, t_4+30 s, t_4+ 40 s , t_4+190 s; (c) Meshed V-shaped intermetallic and the angles between different facets; (d1)Volume change of V-shaped particle as a function of time (d2) Growth velocity of the V-shaped particle.

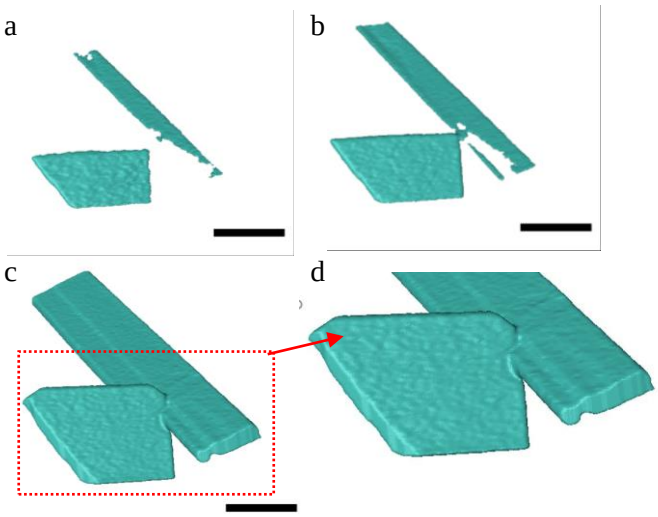

Fig. 11. (a-c) Impingement growth mechanism at t_5 +10 s, t_5 +20 s, t_5 +190 s; scale bar:200µm (d) Enlarged view

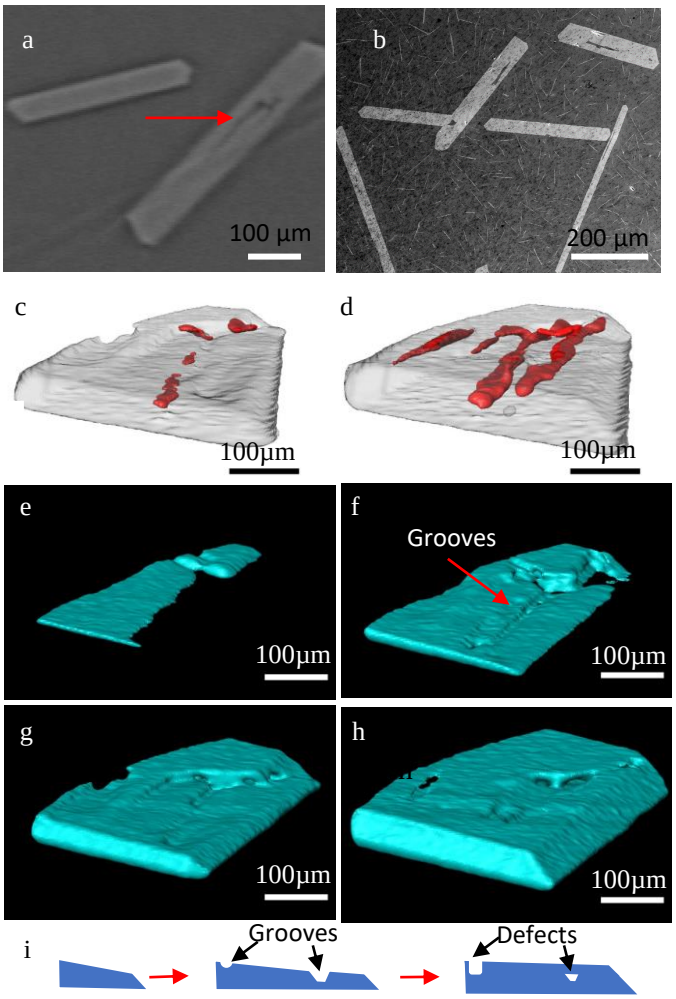

Fig. 12. (a) and (b) 2D slices of the $Al_{13}Fe_4$ particle; (c) and (d) internal defects at t_6 +160 s, t_6 +560 s. scale bar:100μm (e-h) morphology of the crystal with internal defects at t_6+30 s, t_6 +90 s, t_6 +160 s, t_6 +560 s; (i) Schematic diagram of the defects formation process

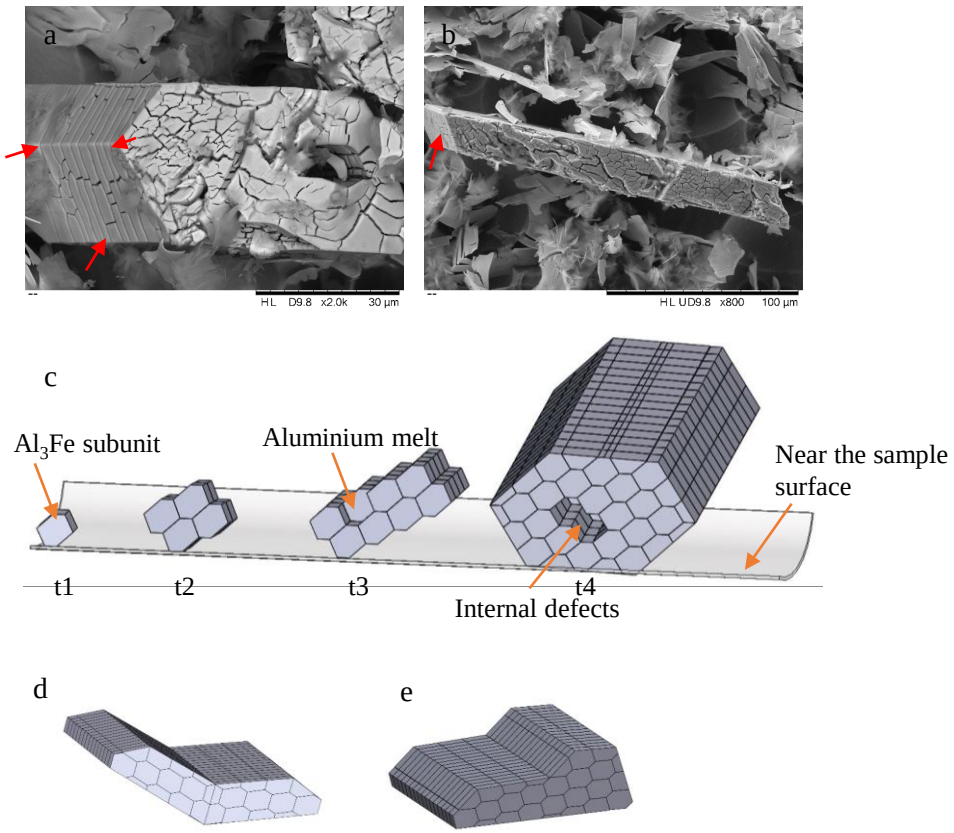

Fig. 13. (a-b) SEM images of $Al_{13}Fe_4$ intermetallics after deep etching; (c) Schematic diagram of the formation mechanism of $Al_{13}Fe_4$, where t1-t4 are at different stages of solidification processes; (d) V-shaped structure; (e) Stair-like structure.